INORGANIC CHEMISTRY FRONTIERS

RESEARCH ARTICLE

View Article Online
View Journal | View Issue

Cite this: *Inorg. Chem. Front.*, 2024, **11**, 172

A latest-generation fluoride with excellent structural stiffness for ultra-efficient photoluminescence and specific four-peak emission temperature sensing†

Kejie Li, Mengmeng Dai, Zuoling Fu, * Zhiying Wang, Hanyu Xu and Rong Wang

Fluorides have garnered tremendous attention in rare-earth-doped fluorescent probes owing to their low phonon energy and excellent optical transparency. However, the latest generation of fluorides, $LiYF_4$, is plagued by extremely complex and uncontrollable synthesis methods, which greatly restricts its further exploration and application. Herein, a straightforward one-step method for the synthesis $LiYF_4:Ln^{3+}$ with micron-sized cones and nano-spheres is reported. Astonishingly, self-sensitized luminescence was achieved under multi-wavelength excitation when Er^{3+} was singly doped. $LiYF_4:Yb^{3+},Er^{3+}$ demonstrated superior luminescence intensity to those of commercial green phosphors ($NaYF_4:Yb^{3+},Er^{3+}$); this ultra-efficient photoluminescence was confirmed from the crystal structure, electronic band properties, morphological analysis and Debye temperature calculations. Further, by constructing cross-relaxation between the Ce^{3+} and Er^{3+} ions ($^4I_{11/2} + {}^2F_{5/2} \rightarrow {}^4I_{13/2} + {}^2F_{7/2}$), the specific four-peak emission (SFPE) intensity of Er^{3+} in NIR-IIb was significantly increased, further enhancing the relative sensitivity of thermally coupled temperature sensing based on SFPE. Subsequently, non-thermally coupled temperature sensing based on SFPE was also achieved through the construction of phonon-assisted energy transfer between Ho^{3+} $^5I_6$ and Er^{3+} $^4I_{13/2}$. In summary, this paper not only puts forward theoretical and experimental arguments for the use of $LiYF_4$ to replace the conventional $NaYF_4$, but also substantiates the extraordinary prospects of $LiYF_4$ as a temperature-sensitive fluorescent probe in nanomedicine.

Received 19th September 2023,
Accepted 3rd November 2023

DOI: 10.1039/d3qi01902k

rsc.li/frontiers-inorganic

1. Introduction

The photoluminescence (PL) efficiency of rare earth ions depends primarily on the crystal field, structure, phonon energy and local positional symmetry of the host material.[1] Amongst these characteristics, phonon energy is a critical component affecting the quantum yield. Hosts having low phonon energy can suppress the multi-phonon relaxation process and reduce non-radiative energy losses.[2] In particular, phonon energy is essential for the emission of rare earth ions in the NIR, as NIR emission is susceptible to being quenched by high-energy vibrations.[3] Therefore, the choice of host determines the optical properties of rare-earth-ion dopants. Rare-earth-ion-doped fluorides have excellent photoluminescence efficiency due to their high photodamage threshold and low phonon energy.[4] Among them, $NaYF_4$ is widely used for rare-earth-doped photoluminescence[5,6] and bioimaging in the NIR due to its outstanding chemical stability and low phonon energy.[7] $NaYF_4$:18%Yb^{3+},2%Er^{3+} is even known as a commercial green phosphor owing to its high-intensity green light emission.[8] However, $LiYF_4$ has received little attention.

As currently reported, $LiYF_4:Nd^{3+}$ has an amazingly high quantum efficiency in the NIR-II (28%) under 808 nm excitation, with relatively stronger emission and higher quantum yields than $NaYF_4$ NPs with the same doping ratio, much higher than any previously reported fluoride.[9] Xiuwen Wang *et al.* investigated the effect of Li^+ ion doping on the morphology, structure and up-conversion luminescence of $NaYF_4:Yb^{3+},Er^{3+}$ nanocrystals and found a significant enhancement of the up-conversion luminescence by Li^+ ion doping,[10] but did not investigate the principle in depth. In fact, $LiYF_4$, a representative fluoride, has the advantage of low phonon energy and optimal optical transparency to minimize non-radiative energy losses. Rare-earth-ion-doped $LiYF_4$ crystals demonstrated superior quantum yields under excitation at 1490 nm compared to $NaYF_4$ crystals.[11] However, the complex synthesis process of $LiYF_4$ and the high operational and environmental requirements have hindered further research.

Coherent Light and Atomic and Molecular Spectroscopy Laboratory, Key Laboratory of Physics and Technology for Advanced Batteries, Jilin University, Changchun 130012, China. E-mail: zlfu@jlu.edu.cn

† Electronic supplementary information (ESI) available. See DOI: https://doi.org/10.1039/d3qi01902k

Among the synthesis methods reported so far, there are thermal decomposition methods that use precise control of the synthesis environment and process,[12,13] two-step synthesis methods that use stepwise regulation of the synthesis of YF_3 and then $LiYF_4$,[14] and improved methods that use special high-pressure steel kettles or rely on high-temperature tube furnaces.[15] In general, the synthesis process is more tedious and technically demanding than for other fluorides, limiting its application to rare-earth-doped luminescence and contactless temperature sensing.

In this work, we have successfully synthesized rare-earth-doped $LiYF_4$ *via* a one-step hydrothermal method. When $LiYF_4$ was singly doped with Er^{3+} ions, it displayed Er^{3+} ion self-sensitization and high-intensity luminescence with multi-wavelength excitation.[16,17] After the introduction of the sensitizer Yb^{3+}, its ultra-efficient photoluminescence was 2.06 times higher than that of commercial green phosphors ($NaYF_4$:Yb^{3+}, Er^{3+}), and the specific four-peak emission (SFPE) in the NIR-IIb was 3.15 times higher than the single-peak emission of commercial green phosphors. Even more surprising is the excellent performance in temperature sensing based on the fluorescence intensity ratio of the two green thermally coupled energy levels (Er^{3+} $^2H_{11/2}$, $^4S_{3/2}$) and SFPE in the NIR-IIb. Subsequently, we co-doped Ce^{3+} ions to achieve a 3.07-fold increase in emission intensity in the NIR-IIb region while achieving a further increase in relative sensitivity. Finally, temperature sensing based on the Ho^{3+} and Er^{3+} energy levels was also achieved. A pathway has been opened for the application of $LiYF_4$ in bioimaging and nanomedicine.

2. Results and discussion

2.1 Structure and composition

The XRD patterns of $LiYF_4$:x%Er^{3+} phosphors (x = 0.6, 0.8, 1.0, 1.2, 1.4, and 1.6) are shown in Fig. 1c; all the diffraction patterns were well matched with the standard reference, indicating that all the generated samples exhibited favorable single phases. Furthermore, as the concentration of Er^{3+} doping increased, the locations of the diffraction peaks in the XRD patterns moved toward smaller angle, revealing that the substitution of Er^{3+} with Y^{3+} resulted in the substitution of an ion with a greater ionic radius. The General Structure Analysis System (GSAS) was used to apply Rietveld analysis to refine the $LiYF_4$:1%Er^{3+} phosphors, as shown in Fig. 1d. The low residual factor parameters (R_p = 6.35%, R_{wp} = 8.77%) demonstrated the high purity of the sample. The simple hydrothermal one-step stable synthesis of rare-earth-doped $LiYF_4$ sets the foundation for our subsequent discussion.

2.1.1 Structural properties. The compound $LiYF_4$ crystallizes in a tetragonal system with the space group $I4_1/a$; the ordered conformation is shown in Fig. 1a, in which Y^{3+} and Li^+ are located at the center of the octa-coordinated dodecahedron [YF_8] and the tetra-coordinated tetrahedron [LiF_4], respectively. Nevertheless, as illustrated in Fig. 1f, α-$NaYF_4$ is a disordered crystal, in which Y^{3+} and Na^+ stochastically take up the cationic position. In the disordered β-$NaYF_4$ crystal (Fig. 1g), there are two Ln^{3+} cation sites; one is occupied by Na^+, and the other one is dominated exclusively by Na^+ and Y^{3+} at random. The sensitizer and activator ions Yb^{3+} (112.5 pm, CN = 8), Er^{3+} (114.4 pm, CN = 8) and Ho^{3+} (115.5 pm, CN = 8) tend to assume the position of Y^{3+} (115.9 pm, CN = 8), forming the luminescence centre in $LiYF_4$ and $NaYF_4$. Therefore, compared to $NaYF_4$:Ln^{3+}, the superior luminescence efficiency for $LiYF_4$:Ln^{3+} is reasonable based on their ordered cation sites.[18] In addition, the Y–Y atomic distance in $LiYF_4$ is shorter compared to those of α-$NaYF_4$ and β-$NaYF_4$, and it is well-known that the closer Ln^{3+} position in the crystal facilitates efficient Ln^{3+}–Ln^{3+} energy transfer and thus yields efficient photoluminescence. The bond lengths of Y–F in $LiYF_4$, α-$NaYF_4$ and β-$NaYF_4$ are 2.214, 4.535 and 2.318 Å, respectively, and the Li/Na–F bond lengths are 1.848, 4.535 and 1.855 Å, respectively (Fig. 1h). With the shorter bond lengths in $LiYF_4$, the bonding forces between the bonded atoms are the stronger, which is also consistent with the fact that the lighter the atoms, the greater the interatomic forces. In terms of structural properties, the better luminous efficiency of $LiYF_4$:Ln^{3+} was justified by its tight lattice structure.[18]

Fig. 1b presents the SEM image of the $LiYF_4$ host, which exhibited excellent dispersion and micron-sized octahedral cones. Here, we present an analysis of the morphological structure of the octahedral conical $LiYF_4$ and the conventional spherical $NaYF_4$; as shown in Fig. S1,† the octahedral cones have an edge length d, volume (V_c), and surface area (S_c):

$$V_c = d^2 \times \frac{d}{\sqrt{2}} \times \frac{1}{3} \times 2 = \frac{\sqrt{2}}{3} d^3 \quad (1)$$

$$S_c = d^2 \times \frac{\sqrt{3}}{4} \times 8 = 2\sqrt{3} d^3 \quad (2)$$

For the traditional spherical $NaYF_4$ with radius r, the volume (V_s), and surface area (S_s) are:

$$V_S = \frac{4}{3}\pi r^3 \quad (3)$$

$$S_S = 4\pi r^2 \quad (4)$$

when $V_s = V_c$:

$$\frac{S_s}{S_c} = \frac{\pi}{\sqrt{3}(\sqrt[3]{\pi})^2} = 0.85 \quad (5)$$

Thus, the octahedral conical $LiYF_4$ has a larger surface area than that of commonly reported sphere-like $NaYF_4$ for an identical volume, which improves the thermal response of their upconversion behavior,[19] and this would further improve the sensitivity of the temperature-sensitive fluorescent probe.

2.1.2 Electronic band properties. A detailed calculation of the energy band properties of $LiYF_4$ was performed to verify whether its electronic structure was suitable to facilitate Ln^{3+} emission. The CASTEP software package in the software

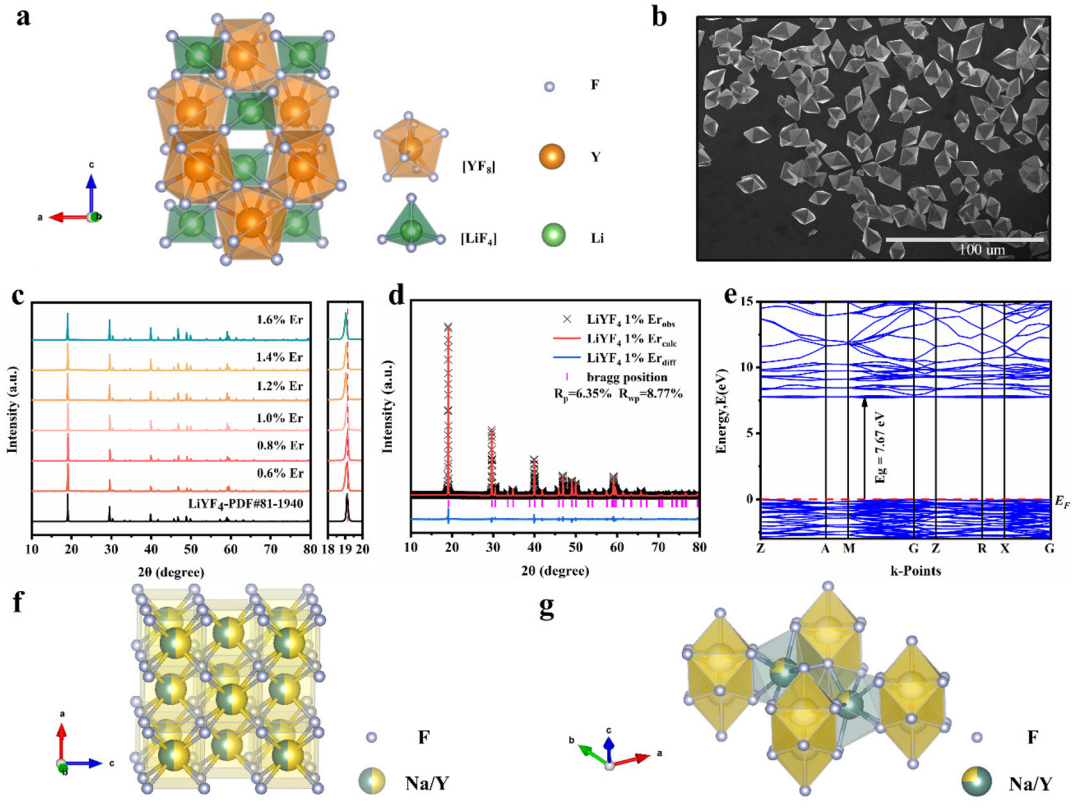

h

$LiYF_4$	(Å)	α-$NaYF_4$	(Å)	β-$NaYF_4$	(Å)
Y_1-F_1	2.214	Y_1-F_1	4.535	Y_1/Na_1-F_1	2.318
Li_1-F_1	1.848	Na_1-F_1	4.535	Na_2-F_1	1.855
Y_1-Y_2	3.612	Y_1-Y_2	3.868	Y_1-Y_2	3.638
	4.959		5.470		3.809

i

C_{ij}	C_{11}	C_{33}	C_{44}	C_{66}	C_{12}	C_{13}	C_{16}
Value	196.51	102.73	83.05	113.74	88.47	68.80	7.46

j

C_{ij}	C_{11}	C_{44}	C_{12}
Value	171.09	78.11	16.42

Fig. 1 (a) Structural model of the $LiYF_4$ host and the F, Y, and Li site positions in the structure. (b) SEM image of the $LiYF_4$ host. (c) XRD patterns of the $LiYF_4$:x%Er^{3+} phosphors, along with the standard XRD data of $LiYF_4$ (PDF 81-1940). (d) XRD Rietveld refinement of $LiYF_4$:1%Er^{3+} phosphors. (e) Energy band structures of the $LiYF_4$ host; the Fermi energy levels are indicated by dashed lines. Schematic illustrations of unit cell structures of α-$NaYF_4$ (f) and β-$NaYF_4$ (g). (h) Bond lengths (Å) in $LiYF_4$, α-$NaYF_4$ and β-$NaYF_4$. Calculation results of the elastic coefficients C_{ij} of $LiYF_4$ (i) and $NaYF_4$ (j).

Materials Studio was used for the calculation. As shown in Fig. 1e, the band gap value of the $LiYF_4$ system was 7.67 eV, which was also very close to the result calculated (7.52 eV) by Yang Xiao *et al.*[20,21] It was further confirmed by the diffuse reflectance spectrum in Fig. S2.† Owing to the photoionization effect, the bandgap is also related to thermal stability and luminous efficiency. Additionally, the photoionization process can be impeded by a wide bandgap. Consequently, the luminescence intensity of phosphors is anticipated to be positively proportional to the bandgap of the host crystal lattice.[22] Based on the unique electronic structure of $LiYF_4$, its wide bandgap of >3.3 eV is advantageous for accommodating the electronic states of the rare-earth-ion luminescence centers. The density of states (DOS) and the partial atomic components (PDOS) of $LiYF_4$ are shown in Fig. S3,† which reveals that the conduction band (CB) was mainly contributed by Li and Y ions, with very little PDOS contribution from the F ions, while the valence band (VB) was mainly contributed by F ions, with very little PDOS contribution from the Li and Y ions, and that while the important interactions between the F 2s and Y 4p orbitals are rarely discussed in the literature, they are also important interaction mechanisms.

2.1.3 Structural stiffness. Crystal structures with higher structural stiffness have weaker phonon energies, which can

limit the electron–phonon coupling effect to some extent, implying a lower probability of non-radiative relaxation.[2] The Debye temperature and Young's modulus E can be used to describe the structural stiffness.[23] The elastic coefficient C_{ij} was calculated using the CASTEP software package, and the calculations for $LiYF_4$ and $NaYF_4$ are displayed in Fig. 1i and j, respectively. Taking $LiYF_4$ as an example, we made continued calculations for its Debye temperature and Young's modulus (E). The stability requirement was determined by measuring the elastic coefficients C_{ij} of the tetragonal phase $LiYF_4$ as follows: $C_{11} > |C_{12}|$, $2C_{13}^2 < C_{33}(C_{11} + C_{12})$, $C_{44} > 0$, and $2C_{16}^2 < C_{66}(C_{11}–C_{12})$, indicating the rationale of the calculation results.

According to the Voigt approximation, the shear modulus G_V and bulk modulus B_V can be expressed in relation to the elastic coefficients C_{ij} of the crystal as:

$$G_V = \frac{1}{15}(2C_{11} + C_{33} - C_{12} - 2C_{13}) + \frac{1}{5}(2C_{44} + C_{66}) \quad (6)$$

$$B_V = \frac{2}{9}\left(C_{11} + C_{12} + 2C_{13} + \frac{1}{2}C_{33}\right) \quad (7)$$

According to the Reuss approximation, the shear modulus G_R and bulk modulus B_R have the following relationships with the elastic compliance coefficients S_{ij} of the crystal:

$$G_R = \frac{15}{4(2S_{11} + S_{33}) - 42(S_{12} + 2S_{13}) + 3(2S_{44} + S_{66})} \quad (8)$$

$$B_R = \frac{1}{(2S_{11} + S_{33}) - 2(S_{12} + 2S_{13})} \quad (9)$$

The compliance coefficient S_{ij} is the inverse matrix of the elasticity coefficient C_{ij}, the Voigt and Reuss equations describe the upper and lower limits of the real crystal constant, respectively, and the crystal modulus is simply the arithmetic average given by Voigt and Reuss, which is also called the Voigt–Reuss–Hill approximation. The calculation formula is as follows:

$$G = \frac{(G_V + G_R)}{2} \quad (10)$$

$$B = \frac{(B_V + B_R)}{2} \quad (11)$$

Young's modulus (E) represents the stiffness of the material and can be further calculated as:

$$E = \frac{9BG}{3B + G} \quad (12)$$

The compressional longitudinal wave velocity (V_P) and transverse wave velocity (V_S) were calculated as:

$$V_P = \sqrt{\frac{B + \frac{4}{3}G}{\rho}} \quad (13)$$

$$V_S = \sqrt{\frac{G}{\rho}} \quad (14)$$

The mean sound velocity V_m can be obtained as:

$$V_m = \left[\frac{1}{3}\left(\frac{2}{V_S^3} + \frac{1}{V_P^3}\right)\right]^{-\frac{1}{3}} \quad (15)$$

The Debye temperature θ_D can be obtained from the average sound speed and Debye approximation:

$$\theta_D = \frac{\hbar}{\kappa}\left[\frac{3n}{4\pi V}\right]^{\frac{1}{3}} V_m \quad (16)$$

where $\hbar$ is the Bronk constant, k is the Boltzmann constant, n is the number of atoms in the protocell, V is the protocell volume, and V_m is the average phonon velocity.

Based on the calculation results, the Young's modulus (E) value of $LiYF_4$ (E_{LiYF_4}) is 164 N m^{-2}, and the Debye temperature (D_{LiYF_4}) is 569 K; this result is very similar to that in the previous literature report (570 K).[24] The Young's modulus (E) of $NaYF_4$ (E_{NaYF_4}) is 136 N m^{-2}, and the Debye temperature (D_{NaYF_4}) is 532 K. $E_{LiYF_4} > E_{NaYF_4}$ and $D_{LiYF_4} > D_{NaYF_4}$; this is also consistent with the fact that the smaller the atomic mass, the greater the interatomic force, and the higher the Debye temperature. This is an important reason for the superior luminescence intensity of $LiYF_4$. It also provided important theoretical support for $LiYF_4$ as a better luminescence host to replace $NaYF_4$.

Furthermore, the Debye temperature is a fixed eigenvalue of a crystal:

$$n_{av} = \frac{1}{\exp(\theta_D/T) - 1} \quad (17)$$

n_{av} is the average phonon number. When $\exp(\theta_D/T) - 1 < 1$, that is, $\exp(\theta_D/T) < 2$, $T > \theta_D$, then the phonon with the largest energy is excited. Low-frequency phonons can be generated at lower temperatures, and there are also less of them overall. As such, the higher Debye temperature has a higher luminous heat quenching temperature caused by multiphonon relaxation, and in theory, the effective temperature sensing range of $LiYF_4$ based on the luminous intensity ratio before the luminescence burst is greater than that of $NaYF_4$.

In parallel, we synthesized α-$NaYF_4$ and β-$NaYF_4$ phosphors using the hydrothermal method. The XRD patterns are shown in Fig. S4.† To experimentally verify our calculations, infrared spectroscopy was carried out. A detailed evaluation of the lattice vibrations of $LiYF_4$, α-$NaYF_4$ and β-$NaYF_4$ is shown in Fig. S5.† The lattice vibrations can be assessed by the absorption positions;[20] the absorption positions of $LiYF_4$ (213, 264, 299 and 339 cm^{-1}) were overall lower than those of α-$NaYF_4$ (324, 409 and 517 cm^{-1}) and β-$NaYF_4$ (250, 330 and 400 cm^{-1}). This was confirmation of the better structural stiffness of $LiYF_4$.

2.2 Photoluminescence (PL) properties

2.2.1 Multiwavelength responsive and high-intensity PL from Er^{3+} ion self-sensitization . Er^{3+}-doped $LiYF_4$ not only achieved self-sensitization, but also exhibited excellent luminescence properties under multiwavelength excitation. Under excitation at 980, 808 and 381 nm, the red emissions centered at 653 and 667 nm were assigned to the $^4F_{9/2}$ energy level split, and the green emissions centered at 523–529 nm and 542–550 nm were ascribed to the $^2H_{11/2}$-energy level split and $^4S_{3/2}$ energy level split; the SFPE in the NIR-IIb under 808 and 980 nm excitation was attributed to the $^4I_{13/2}$ energy level split. The emission spectra are shown in Fig. 2a and b (at 980 nm), Fig. 2c and d (at 808 nm) and Fig. 2f (at 381 nm). The ideal doping concentrations for the Er^{3+} emissions at the three excitation wavelengths were 1% for the visible region emission and 1.4% for the NIR. The emission slopes of the $LiYF_4$:1% Er^{3+} phosphor at 529, 550, 667 and 1545 nm under 980 nm excitation in Fig. S6a and c† were 2.12, 2.04, 1.97 and 0.95, respectively. The green and red emission were two-photon processes and NIR emission was a single-photon process based on the fitted slope value n ($I \propto P^n$), and the energy conversion mechanism at 980 nm excitation is shown in Fig. 3b. Equally, the green and red emission of the Er^{3+} ions under 808 nm excitation were also two-photon processes (Fig. S6b†), and the NIR emission was a single-photon process (Fig. S6c†), with the energy conversion mechanism shown in Fig. 3c. Subsequently, we also examined the excitation spectra at 552 nm, as shown in Fig. 2e. The excitation spectra show centres at 361, 381, 414, 426 and 452 nm, corresponding to the well-known Er^{3+} ion $^4I_{15/2} \rightarrow {}^4G_{9/2}$, $^4I_{15/2} \rightarrow {}^4G_{11/2}$, $^4I_{15/2} \rightarrow {}^2H_{9/2}$, $^4I_{15/2} \rightarrow {}^4F_{9/2}$, $^4I_{15/2} \rightarrow {}^4F_{3/2}$, $^4I_{15/2} \rightarrow {}^4F_{5/2}$ and $^4I_{15/2} \rightarrow {}^4F_{7/2}$ transitions,[25] respectively. Here, we used the highest absorption peak wavelength of 381 nm for excitation and obtained the emission spectra shown in Fig. 2f. Different from the excitation at 980 nm and 808 nm, the red and green light emission corresponded to single-photon processes, and the energy conversion mechanism is shown in Fig. 3d. Furthermore, we monitored the diffuse reflectance spectra of $LiYF_4$ and $LiYF_4$:1%Er^{3+} as shown in Fig. S7,† and the characteristic peaks of Er^{3+} ions that appeared in comparison to those of the $LiYF_4$ matrix further validated its excellent self-sensitized luminescence properties.

In addition, we further analyzed the SFPE of $LiYF_4$:x%Er^{3+} in the NIR-IIb; it was mainly due to the splitting of the ground state $^4I_{15/2}$ and excited state $^4I_{13/2}$ into multiple Stark sub-levels by the action of the crystal field. The electronic transitions from the $^4I_{13/2}$ to the $^4I_{15/2}$ energy levels of Er^{3+} ions involve intra-configurational transitions within the $4f^N$ configuration, known as 4f–4f transitions. These transitions are not induced by electric dipole interactions because the parity of states within the $4f^N$ configuration is the same, resulting in a zero value for the matrix elements of electric dipole transitions between these states. Consequently, transitions between energy levels within the $4f^N$ configuration are parity-forbidden. However, 4f–5d transitions are allowed, as the matrix elements of electric dipole transitions between these levels are non-zero. Odd-rank crystal field terms can mix configuration states with opposite parity to the $4f^N$ configuration, such as $4f^{N-1}5d$ or $4f^{N-1}5g$ configurations. However, crystallographic point groups with inversion symmetry, like C_{4h}, do not have odd-rank crystal field terms, and according to the selection rules for rare-earth-ion electric dipole transitions in crystals: $\Delta l = \pm 1$, $\Delta S = 0$, $|\Delta L| \leq 6$, $|\Delta J| \leq 6$, when J or $J' = 0$, $|\Delta J| = 2, 4, 6$, $|\Delta M| = p + q$, electric dipole transitions from the $^4I_{13/2}$ to $^4I_{15/2}$ energy levels of Er^{3+} ions are forbidden.

In these 4f–4f transitions, magnetic dipole and electric quadrupole transitions are also significant. Based on the selection rules for magnetic dipole transitions: $\Delta l = 0$, $\Delta S = 0$, $\Delta L = 0$, $|\Delta J| = 0, \pm 1$, $\Delta M = 0, \pm 1$, and electric quadrupole transitions: $\Delta l = 0$, $\Delta S = 0$, $\Delta L \leq 2$, $\Delta J \leq 2$, transitions involving magnetic dipole and electric quadrupole moments from the $^4I_{13/2}$ to $^4I_{15/2}$ energy levels of Er^{3+} ions are allowed. Generally, the energy level splitting of rare earth ions can be decomposed based on the irreducible representation of the point group, using the character of the irreducible representation of the point group to approximate the character of the rotational group representation. This decomposition process was exactly the same as that of the energy levels, because the irreducible representation of the point group in the crystal was actually the quantum number that can completely determine the state,

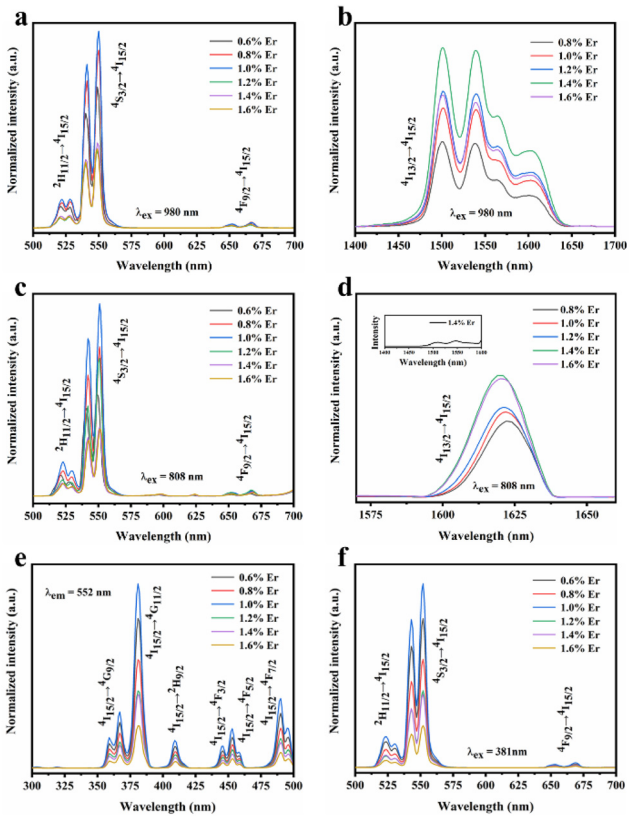

Fig. 2 (a) Visible PL spectra and (b) NIR PL spectra of $LiYF_4$:x%Er^{3+} under 980 nm excitation. (c) Visible PL spectra and (d) NIR PL spectra of $LiYF_4$:x%Er^{3+} under 808 nm excitation. (e) PLE (λ_{em} = 552 nm) and (f) PL spectra (λ_{ex} = 381 nm) of $LiYF_4$:x%Er^{3+}.

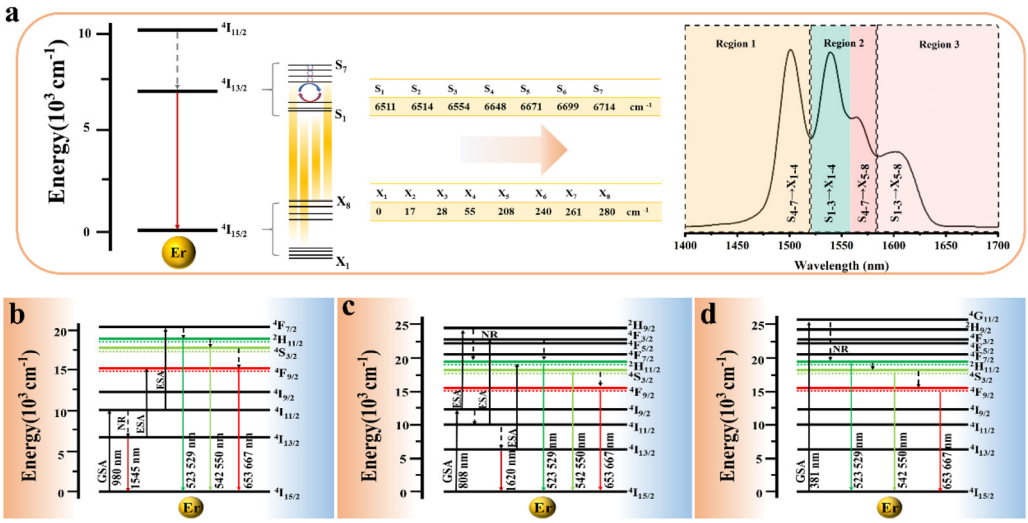

Fig. 3 (a) Stark sublevels of the $^4I_{13/2}$ and $^4I_{15/2}$ levels of the Er^{3+} ions in the $LiYF_4$ host, and the transition of each Stark sublevel corresponding to the SFPE of $LiYF_4$:1.4%Er^{3+} under 980 nm excitation. Energy transfer mechanism of $LiYF_4$:Er^{3+} under 980 nm (b), 808 nm (c), and 381 nm (d) excitation.

and it had the same nature as the angular momentum quantum number in the three-dimensional rotational group, which can characterize the states and energy levels of the rare earth ions in the crystal. The character of the rotational group representation under various symmetry operations can be calculated using the following formula:

$$\chi[D_J^{\pm}(R_\theta)] = \frac{\sin\left(J+\frac{1}{2}\right)\theta}{\sin\left(\frac{\theta}{2}\right)} \quad (18)$$

In the formula, + indicates even parity, and − indicates odd parity. R_θ represents the θ angles along the axis of rotation. J is the total angular momentum of the rare earth energy levels. The character represented by any rotation group of J can be computed using this formula. Then, the character of the rotation group is obtained, and the character of the point group irreducible representation is used to decompose the character of the rotation group representation. The number of irreducible representations of the point group contained in the obtained rotation group representation is the number of Stark levels decomposed by the J level in the point group. $LiYF_4$ has the $I4_1/a$ space group, which belongs to the C_{4h} point group. $C_{4h} = C_4 \times C_i$; it can be viewed as direct product of the group C_4 and the group C_i. The decomposition of the rotation group in this point group is obtained by the compatibility relation between the irreducible representations of these two groups, and the process can be referred to Table S1.† We eventually found the number of Stark levels of the $^4I_{13/2}$ (J = 13/2) level and the $^4I_{15/2}$ (J = 15/2) level for the Er^{3+} ion to be 7 and 8, respectively (marked as $S_1 \rightarrow S_7$, $X_1 \rightarrow X_8$), which is consistent with the calculation of the Harry Diamond Laboratories using diagonalization of the Hamiltonian.[26] Based on these specific calculation results of the Stark levels of $^4I_{13/2}$ and Stark levels of $^4I_{15/2}$ ($S_1 \rightarrow S_7$: 6511, 6514, 6554, 6648, 6671, 6699, 6714 cm^{-1}; $X_1 \rightarrow X_8$: 0, 17, 28, 55, 208, 240, 261, 280 cm^{-1}), and according to the difference in wavenumbers between the various Stark energy levels, we have drawn the transition energy level diagram of SFPE, as shown in Fig. 3a, corresponding to the emission spectrum, with the four parts from left to right coming from $S_{4-7} \rightarrow X_{1-4}$, $S_{1-3} \rightarrow X_{1-4}$, $S_{4-7} \rightarrow X_{5-8}$ and $S_{1-3} \rightarrow X_{5-8}$, respectively. The SFPE in NIR-IIb opens the possibility for the following temperature sensing applications at both thermally coupled Stark sub-levels and non-thermally coupled levels.

2.2.2 Luminescence enhancement and ultra-efficient PL. We further demonstrated the superior luminous intensity of $LiYF_4$ with the introduction of the sensitizer Yb^{3+} due to its higher structural stiffness. Fig. S8a† presents the XRD images of $LiYF_4$:18%Yb^{3+},x%Er^{3+} (x = 1, 2, 3, 4, 5). The emission spectra in the visible range and NIR-IIb are presented in Fig. S8b, c,† and the optimal doping concentration was 18% Yb^{3+},2%Er^{3+} in the visible region and 18%Yb^{3+},3%Er^{3+} in the NIR-IIb. After the incorporation of the sensitizer, there was a 9.60-fold improvement in the visible region and 5.76-fold enhancement in the NIR-IIb region. The emission intensity of β-$NaYF_4$:18%Yb^{3+},2%Er^{3+} (commercial phosphors) and $LiYF_4$:18%Yb^{3+},2%Er^{3+} phosphors was compared. It was clear that the ultra-efficient green emission of the $LiYF_4$:18% Yb^{3+},2%Er^{3+} phosphors was outstanding, as it was 2.06 times higher than that of commercial β-$NaYF_4$:18%Yb^{3+},2%Er^{3+} phosphors (Fig. 4a). The NIR-IIb emission intensity of the $LiYF_4$:18%Yb^{3+},2%Er^{3+} phosphor was also excellent, being 3.15 times stronger than that of β-$NaYF_4$:18%Yb^{3+},2%Er^{3+} phosphors; that of $LiYF_4$:18%Yb^{3+},3%Er^{3+} was 3.75 times that of β-$NaYF_4$:18%Yb^{3+},2%Er^{3+} (Fig. 4b). Furthermore, the SFPE of $LiYF_4$:18%Yb^{3+},3%Er^{3+} in NIR-IIb made it possible to use for thermally coupled temperature sensing at the Stark level.

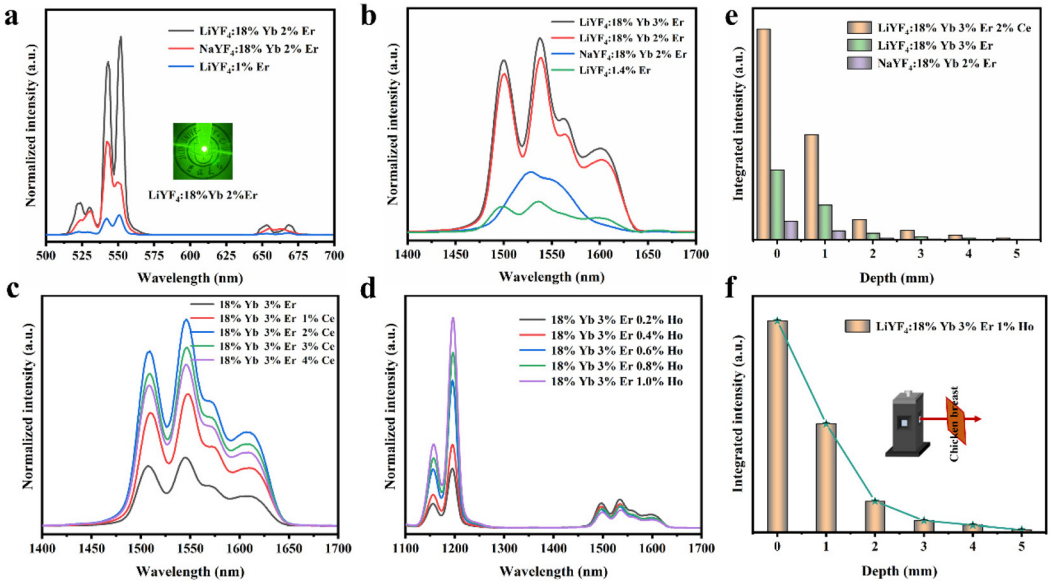

Fig. 4 (a) Up-conversion spectra (visible region) of $LiYF_4$:2%Er^{3+}, $LiYF_4$:18%Yb^{3+},2%Er^{3+} and $NaYF_4$:18%Yb^{3+},2%Er^{3+} under 980 nm excitation. (b) NIR down-conversion spectra of $LiYF_4$:1.4%Er^{3+}, $LiYF_4$:18%Yb^{3+},2/3%Er^{3+} and $NaYF_4$:18%Yb^{3+},2%Er^{3+} under 980 nm excitation. (c) NIR down-conversion spectra of $LiYF_4$:18%Yb^{3+},2%Er^{3+},*x*%Ce^{3+} under 980 nm excitation. (d) Down-conversion spectra (NIR) of $LiYF_4$:18%Yb^{3+},2%Er^{3+},*x*%Ho^{3+} under 980 nm excitation. The emission integrated intensity at 1400–1700 nm (e) and 1100–1700 nm (f) in different depths of chicken breast.

To further improve the NIR emission, two separate ion doping systems were constructed. Fig. S9† depicts the XRD results of $LiYF_4$:18%Yb^{3+},3%Er^{3+},*x*%Ce^{3+} (*x* = 1, 2, 3 and 4), and Fig. 4c presents the NIR-IIb emission spectrum under 980 nm excitation, with the emission intensity peaking at 2% Ce^{3+} doping. The intensity of the NIR-IIb emission was increased by a coefficient of 3.07 compared to that of $LiYF_4$:18%Yb^{3+},3%Er^{3+}. This was attributed to the cross-relaxation between Er^{3+} and Ce^{3+} ions ($^4I_{11/2} + {}^2F_{5/2} \rightarrow {}^4I_{13/2} + {}^2F_{7/2}$), causing a further increase in the $^4I_{13/2}$ (Er^{3+}) energy level population. However, the cross-relaxation between Ce^{3+} ions increased as the Ce^{3+} ion concentration increased, and the optimum doping concentration was found to be 2%. Following this, the depth of penetration of $LiYF_4$:18%Yb^{3+},3%Er^{3+},2% Ce^{3+} in chicken breasts was explored to illustrate their significant potential for bioimaging. As shown in Fig. S10a,† with the increased depth of the chicken breast, the emission intensity diminishes considerably. Compared with the penetration depth of $LiYF_4$:18%Yb^{3+},3%Er^{3+} (4 mm) and β-$NaYF_4$:18% Yb^{3+},2%Er^{3+}(3 mm), $LiYF_4$:18%Yb^{3+},3%Er^{3+},2%Ce^{3+} achieved a depth of 5 mm (Fig. 4e). Subsequently, using co-doping with Ho^{3+} ions, it was investigated whether the energy transfer (as depicted in Fig. 6g) between the Ho $^5I_6$ and $^5I_7$ energy levels and the Er $^4I_{13/2}$ energy levels played a role in promoting the NIR-IIb emission of the Er^{3+} ions. $LiYF_4$:18%Yb^{3+}, 3%Er^{3+},*x*% Ho^{3+} (*x* = 0.2, 0.4, 0.6, 0.8 and 1.0) were prepared. Their XRD patterns are shown in Fig. S9b,† and their NIR emission spectra under 980 excitation are shown in Fig. 4d. On one hand, the probability of phonon-assisted energy transfer was relatively lower because phonon energy was not excited in large quantities at room temperature, and the energy level difference between Er $^4I_{13/2}$ and Ho $^5I_7$ (1494 cm^{-1}) was less than that of Ho $^5I_6$ to Er $^4I_{13/2}$ (2004 cm^{-1}), of which the former energy transfer played a dominant role. On the other hand, there was competition between the Yb–Er and Yb–Ho energy transfer. As a result, the SFPE intensity of the Er^{3+} ions decreased with increasing doping concentration of Ho^{3+} ions. Despite this, $LiYF_4$:18%Yb^{3+},2%Er^{3+},1%Ho^{3+} also penetrated to a depth of 5 mm (Fig. 4f) and the PL spectra for different depths of chicken breast are shown in Fig. S10b.† The tremendous promise of $LiYF_4$ in the bioimaging field was demonstrated.

2.3. Temperature sensing performance

2.3.1 Temperature sensing in the visible region. Temperature sensing based on luminous intensity ratio (LIR) technology[27] is one of the most popular non-contact temperature detection methods.[28] Fig. S15† presents the experimental equipment schematic for temperature sensing. The two green photothermal thermally coupled levels of Er^{3+} ($^2H_{11/2}$, $^4S_{3/2}$) are usually used as the two energy levels for temperature sensing. Here, the $LiYF_4$:18%Yb^{3+},3%Er^{3+} phosphors were excited at 980 nm. In the visible region, the ratio of the signals of the $^2H_{11/2}$ and $^4S_{3/2}$ levels of Er^{3+} were chosen for the following temperature sensing experiments. Fig. 5a shows the green emission spectra at various temperatures. The variation of the integral of the emission intensity with temperature for the thermally coupled levels in the $LiYF_4$:18%Yb^{3+},3%Er^{3+} phosphor is shown in Fig. 5b; a significant difference can be found in the fact that the average integral intensity of the $^4S_{3/2} \rightarrow {}^4I_{15/2}$ (550 nm) transition decreased more rapidly than that of the $^2H_{11/2} \rightarrow {}^4I_{15/2}$ (529 nm) transition. The relative popu-

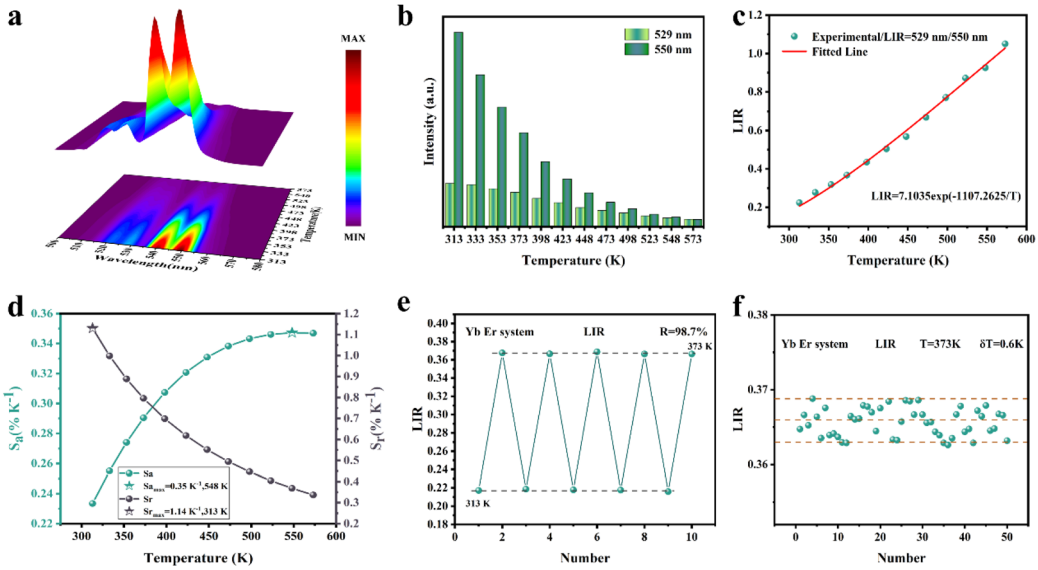

Fig. 5 (a) Temperature-dependent upconversion (UC) emission spectra of $LiYF_4$:18%Yb^{3+},3%Er^{3+}. (b) Summary of the integrated intensity of the emission of the thermally coupled levels in the $LiYF_4$:18%Yb^{3+},3%Er^{3+} phosphors at different temperatures. (c) LIR values related to the temperature. (d) S_r/S_a-temperature curve of $LiYF_4$:18%Yb^{3+},3%Er^{3+}. (e) LIR repeatability over five heating–cooling cycles. (f) LIR values measured 50 times continuously at 373 K.

lation of thermally coupled levels was compatible with the Boltzmann distribution law, which can be calculated using eqn (19):[29]

$$\mathrm{LIR} = \frac{I_{529}}{I_{550}} = B\exp\left(\frac{-\Delta E}{kT}\right) \tag{19}$$

where I_{529} and I_{550} represent the integral emission intensities of Er^{3+} ($^2H_{11/2}$ and $^4S_{3/2}$), and B is a fitted parameter. ΔE is the energy difference between $^2H_{11/2}$ and $^4S_{3/2}$. k is the Boltzmann constant, and T is the absolute temperature. As presented in Fig. 5c, the values of B and $\Delta E/k$ were 7.1035 and 1107.2625, respectively.

According to previous reports, in order to better evaluate and compare the temperature measurement capabilities of different thermometers, quantitative comparisons are usually made using absolute sensitivity (S_a) and relative sensitivity (S_r), which can be estimated using the following expressions:

$$S_a = \left|\frac{\partial \mathrm{LIR}}{\partial T}\right| = \mathrm{LIR}\left(\frac{\Delta E}{kT^2}\right) = B\left(\frac{\Delta E}{kT^2}\right)\exp\left(\frac{\Delta E}{kT}\right) \tag{20}$$

$$S_r = \left|\frac{1}{\mathrm{LIR}}\frac{\partial \mathrm{LIR}}{\partial T}\right| = \frac{\Delta E}{kT^2} \tag{21}$$

As shown in Fig. 5d, S_a and S_r have a high degree of fitting accuracy. However, regardless of the physical mechanism of the luminous thermometer, it is not reliable to use S_a to assess its temperature measurement performance.[30] Instead, S_r should be used for comparison. Nevertheless, the maximum S_a (0.35%) of the phosphor was not very low. The $LiYF_4$:18% Yb^{3+}, 3%Er^{3+} phosphor exhibits excellent S_r ($1107/T^2$), reaching a maximum of 1.14% K^{-1} at 313 K, showing excellent accuracy compared to those in other luminescent materials that utilize the Er^{3+} thermally coupled levels for temperature measurement (Table 1). In addition, we performed five more heating–cooling cycles to investigate the effect on its LIR repeatability, as shown in Fig. 5e. R can be used to describe the ability of a thermometer to provide the same result repeatedly in the same environment and is calculated as:

Table 1 Comparison of the temperature measurement performance of different materials

Compound	λ_{ex} (nm)	λ_{em} (nm)	Temperature (K)	S_r ($\%K^{-1}$)	Ref.
$NaYF_4$:Yb,Er	980	522/553	160–320	$1082/T^2$	31
LaF_3:Yb,Er	980	523/545	150–400	$844/T^2$	32
$CaWO_4$:Yb,Er	980	521/548	300–530	$946/T^2$	33
Gd_2O_3:Yb,Er	980	522/546	300–900	$746/T^2$	34
$LiYF_4$:Yb,Er	980	529/550	313–573	$1107/T^2$	This work

$$R = 1 - \frac{\max(|\mathrm{LIR_c} - \mathrm{LIR}_i|)}{\mathrm{LIR_c}} \tag{22}$$

where LIR_c is the standard value extracted from the calibration curve and LIR_i is the value for each measurement. R was 98.7%, which indicated that our phosphors have good reproducibility. The $LiYF_4$:18%Yb^{3+},3%Er^{3+} phosphors were measured 50 times continuously at 373 K to study the temperature uncertainty (δT), as shown in Fig. 5f. The temperature uncertainty (δT) is a critical property for measuring temperature readout performance and can be calculated according to eqn (23):

$$\delta T = \frac{1}{S_r}\frac{\delta \mathrm{LIR}}{\mathrm{LIR}} \tag{23}$$

here δLIR is the standard deviation of the LIR, and δLIR/LIR is the relative uncertainty of the LIR, depending on the material used and the experimental testing device. The value of temperature uncertainty (δT) was calculated to be very small at 0.6 K, which demonstrates the excellent accuracy of the temperature measurement.

2.3.2 Temperature sensing in the NIR-IIb. We produced $LiYF_4$:18%Yb^{3+},3%Er^{3+}, $LiYF_4$:18%Yb^{3+},3%Er^{3+}, 0.2%Ho^{3+} and $LiYF_4$:18%Yb^{3+},3%Er^{3+},2%Ce^{3+} nanospheres with a size of about 205 nm by optimizing the synthesis process, which makes it possible to use $LiYF_4$ in nanomedicine. The XRD patterns are shown in Fig. S11a,† and the SEM images are shown in Fig. S11b–d.† We divided the SFPE in the NIR-IIb into three regions (region 1: $S_{4-7} \rightarrow X_{1-4}$, region 2: $S_{1-3} \rightarrow X_{1-4}$ and $S_{4-7} \rightarrow X_{5-8}$, region 3: $S_{1-3} \rightarrow X_{5-8}$) for convenience in the following temperature sensing. Fig. 6a presents the temperature-dependent NIR-IIb emission spectra of $LiYF_4$:18%Yb^{3+},3%Er^{3+}. The increase in temperature caused spectral broadening and a blue-shift in the position of the emission peak in region 1, as illustrated in Fig. S13.† This was mostly due to the fact that the $^4I_{13/2}$ Stark sublevels S_{1-3} and S_{4-7} follow the Boltzmann thermal distribution, causing the number of S_{4-7} electrons to rise with temperature. S_4 to S_7 also satisfy the Boltzmann thermal distribution, so that the electrons continue to be distributed to higher energy levels, causing the blue shift of the peak position and spectral broadening. Then, thermal quenching brought on by an increase in temperature was responsible for the decrease in peak intensity. At the same time, the emission integral intensity of region 1 ($S_{4-7} \rightarrow X_{1-4}$) increased with increasing temperature (Fig. S12a†). This was due to the fact that the Stark sublevels X_{1-4} and X_{4-5} of $^4I_{15/2}$ also conform to the Boltzmann redistribution, resulting in the continuous decrease in the number of X_{1-4} electrons, but an increasing number of electrons in S_{4-7}, giving a greater chance of a transition from S_{4-7} to X_{1-4}. On the contrary, the emission integral intensity of region 3 ($S_{1-3} \rightarrow X_{5-8}$) decreased with increasing temperature (Fig. S12a†). This was because S_{1-3} and S_{4-7}, X_{1-4} and X_{5-8} follow the Boltzmann thermal distribution, which led to a continuous decrease in the number of S_{1-3} electrons and the continuous saturation of X_{5-8} electrons, decreasing the likelihood of the transition from S_{1-3} to X_{5-8}. Using eqn (19), the LIR (region 1: $S_{4-7} \rightarrow X_{1-4}$/ region 3: $S_{1-3} \rightarrow X_{5-8}$) values can be calculated, and they are given in Fig. 6d. The S_a and S_r values were calculated, as

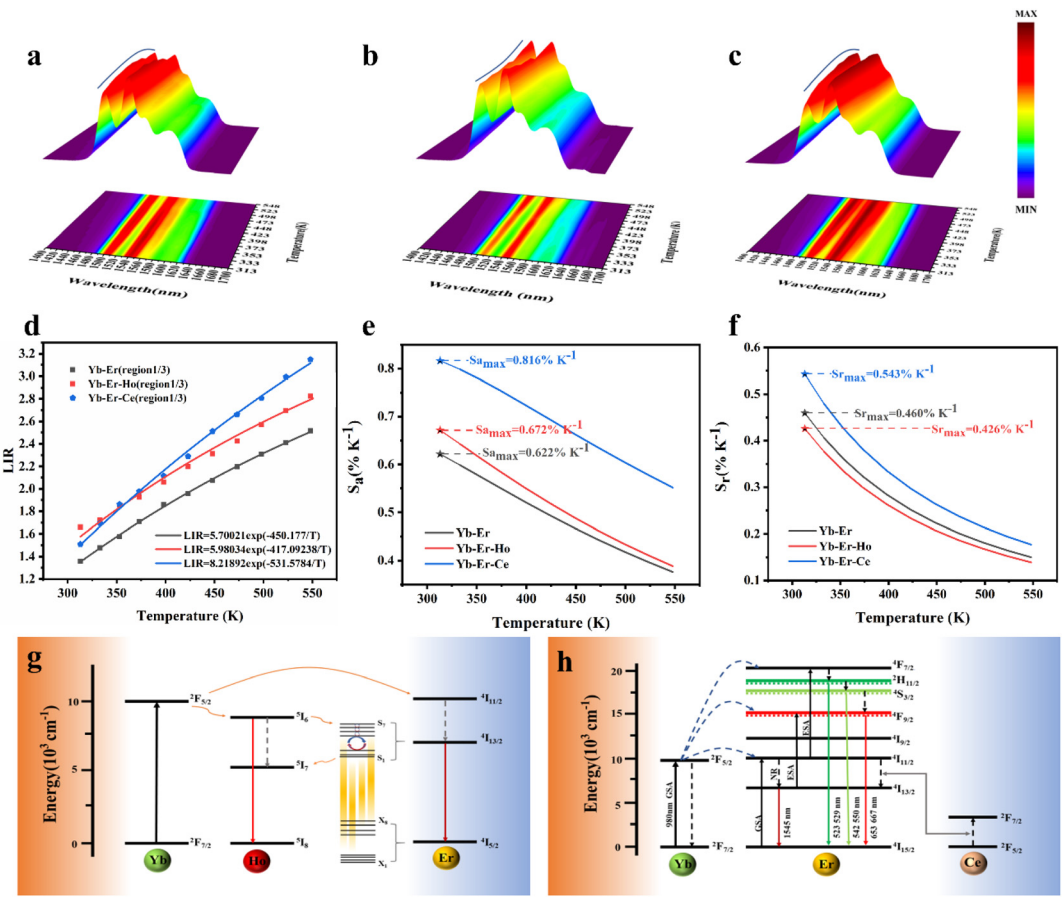

Fig. 6 Temperature-dependent NIR-IIb emission spectra of $LiYF_4$:18%Yb^{3+},3%Er^{3+} (a), $LiYF_4$:18%Yb^{3+},3%Er^{3+},0.2%Ho^{3+} (b), and $LiYF_4$:18%Yb^{3+},3%Er^{3+},2%Ce^{3+} (c). (d) LIR values as a function of temperature for Yb–Er, Yb–Er–Ho and Yb–Er–Ce. (e) S_a-temperature curve. (f) S_r-temperature curve. Energy transfer mechanisms of Yb–Er–Ho (g) and Yb–Er–Ce (h) under 980 nm excitation.

shown in Fig. 6e, f and it was found that $S_{a\ max}$ = 0.622% K^{-1} (T = 313 K), while the S_r value was $450/T^2$ with $S_{r\ max}$ = 0.460% K^{-1} (T = 313 K); this is higher than that of $NaScF_4$:Yb^{3+},Er^{3+} ($313/T^2$), which is one of the few substrates with SFPE in the NIR-IIb region, and even higher than that after increasing S_r ($340/T^2$) by re-doping with Mn^{2+} ions ($NaScF_4$:Yb^{3+},Er^{3+},Mn^{2+}).[35]

The SFPE intensity of the Er^{3+} ions decreased with increasing doping concentration of Ho^{3+} ions, as shown in Fig. 4d, so Li-YF_4:18%Yb^{3+},3%Er^{3+},0.2%Ho^{3+} was selected to continue the temperature sensing study in the NIR-IIb. The temperature-dependent NIR-IIb emission spectra of $LiYF_4$:18%Yb^{3+},3% Er^{3+},0.2%Ho^{3+} are shown in Fig. 6b. With increasing temperature, the emission peak position of region 1 was blue shifted, and the spectrum was broadened. Unlike in the case of $LiYF_4$:18%Yb^{3+},3%Er^{3+}, the emission peak intensity continued to increase with increasing temperature as a result of the continuous replenishment of the $^5I_6$ level of the Ho^{3+} ions to the S_{4-7} level of the Er^{3+} ions, which cancels out the influence of thermal quenching on it. As shown in Fig. S12b,† region 1 had an increase in comprehensive intensity. Fig. 6g illustrates the energy transfer method. The ground-state $^2F_{7/2}$ electrons of the Yb^{3+} ions absorbed the 980 nm photon energy to transition to the excited state $^2F_{5/2}$ level, and the energy was transferred to the activators so that the ground-state electrons of the Ho^{3+} ions and Er^{3+} ions absorbed energy to transition to the Ho^{3+}–$^5I_6$ and Er^{3+}–$^4I_{11/2}$ levels. Then, the 1200 nm NIR-IIa emission of the Ho^{3+} ions was generated. In contrast, the electrons of the Er^{3+} $^4I_{11/2}$ level reached the Er^{3+} $^4I_{13/2}$ level through non-radiative relaxation, and the $^4I_{13/2}$ → $^4I_{5/2}$ electron transition produced the SFPE in the NIR-IIb of the Er^{3+} ions. However, as shown in Fig. 6g, there was energy transfer between the Ho^{3+} $^5I_6$ and $^5I_7$ levels and the Stark sublevels S_{1-3} and S_{4-7} of the Er^{3+} $^4I_{13/2}$ level, which breaks the thermal coupling distribution between the Stark sublevels of the Er^{3+} ions, and this is a possible cause of the slight decrease in S_r. Fig. 6d shows the LIR (region 1: S_{4-7} → X_{1-4}/region 3: S_{1-3} → X_{5-8}) fitting curve. The maximum S_a value of the $LiYF_4$:18%Yb^{3+},3%Er^{3+},0.2%Ho^{3+} nanospheres was 0.672% K^{-1} (T = 313 K) (Fig. 6e), and the S_r value was $417/T^2$ with $S_{r\ max}$ = 0.426 K^{-1} (T = 313 K) (Fig. 6f). Although the value of S_r was lower than that without Ho^{3+} doping, it was still higher than that of $NaScF_4$:Yb^{3+},Er^{3+}. Furthermore, it provided the possibility for subsequent temperature sensing in the NIR-IIa and NIR-IIb.

$LiYF_4$:18%Yb^{3+},3%Er^{3+},2%Ce^{3+} nanospheres were again selected for temperature sensing research. The temperature-dependent NIR-IIb emission spectra of $LiYF_4$:18%Yb^{3+},3% Er^{3+},2%Ce^{3+} are presented in Fig. 6c, and the energy transfer mechanism is shown in Fig. 6h. Cross relaxation between the Ce^{3+} ions and Er^{3+} ions ($^4I_{11/2\ (Er^{3+})}$ + $^2F_{5/2\ (Ce^{3+})}$ → $^4I_{13/2\ (Er^{3+})}$ + $^2F_{7/2\ (Ce^{3+})}$) was brought about by the doping of Ce^{3+} ions and was primarily responsible for the amplification of the SFPE intensity of the Er^{3+} ions in the NIR-IIb. Because of this, the number of electrons at the $^4I_{13/2}$ level was only increased and there was no energy transfer with the thermally coupled S_{1-7} Stark sublevels of Er^{3+} as in the case of Ho^{3+} ions, which led to a more pronounced increase in the integrated intensity of region 1 and a more significant decrease in the integrated intensity of region 3 with increasing temperature (Fig. S13c†). The LIR (region 1: S_{4-7} → X_{1-4}/region 3: S_{1-3} → X_{5-8}) values as a function of temperature are shown in Fig. 6d. The S_a and S_r values were calculated, and I was found that $S_{a\ max}$ = 0.816% K^{-1} (T = 313 K), and the S_r was $532/T^2$ with $S_{r\ max}$ = 0.543% K^{-1} (T = 313 K) (Fig. 6e and f). S_a and S_r were significantly improved compared with those of $LiYF_4$:18%Yb^{3+},3%Er^{3+}. This showed the excellent accuracy compared to luminescent materials that use thermal coupling levels for temperature measurements in the NIR (Table 2).

In addition, the results of LIR repeatability over five heating–cooling cycles and 50 consecutive measurements of the LIR value at 333 K are shown in Fig. S14a and b.† The R values of $LiYF_4$:18%Yb^{3+},3%Er^{3+}, $LiYF_4$:18%Yb^{3+},3%Er^{3+},0.2% Ho^{3+} and $LiYF_4$:18%Yb^{3+},3%Er^{3+},2%Ce^{3+} were 99.7%, 99.6% and 99.7%, respectively, and the temperature uncertainty (δT) was 1.4 K, 1.3 K and 0.3 K, respectively. Once again, the SFPE was shown to have an excellent performance as a temperature sensor.

2.3.3 Temperature sensing in the NIR-IIa and NIR-IIb. We tried to use the SFPE of Er^{3+} for non-thermal coupling temperature measurement. The emission spectra of the $LiYF_4$:18% Yb^{3+},3%Er^{3+},0.2%Ho^{3+} nanospheres excited at 980 nm with temperature change are shown in Fig. 7a. As the temperature rose, the emission intensity of Ho^{3+} ion $^5I_6$ level at 1200 nm in the NIR-IIa decreased, while the SFPE intensity of the Er^{3+} ion $^4I_{13/2}$ level in the NIR-IIb remained stable and even increased

Table 2 Comparison of the temperature measurement performance of different materials

Compound	λ_{ex} (nm)	Stark transition	Temperature (K)	S_r (%K^{-1})	Ref.
$NaScF_4$:Yb/Er	980	Er^{3+}:$^4I_{13/2}$ → $^4I_{15/2}$	298–333	$313/T^2$	35
$NaScF_4$:Yb/Er/Mn	980	Er^{3+}:$^4I_{13/2}$ → $^4I_{15/2}$	298–333	$340/T^2$	35
$BaMoO_4$:Yb/Er	980	Er^{3+}:$^4I_{13/2}$ → $^4I_{15/2}$	293–553	$110/T^2$	36
TiO_2:Yb/Er	980	Er^{3+}:$^4F_{9/2}$ → $^4I_{15/2}$	307–673	$107/T^2$	37
$NaYbF_4$:Tm	980	Tm^{3+}:$^3H_4$ → $^3H_6$	10–295	$10^2/T^2$	38
CaF_2:Nd/Y	800	Nd^{3+}:$^4F_{3/2}$ → $^4I_{11/2}$	300–335	$190/T^2$	39
$LiYF_4$:Yb/Er	980	Er^{3+}:$^4I_{13/2}$ → $^4I_{15/2}$	313–548	$450/T^2$	This work
$LiYF_4$:Yb/Er/Ho	980	Er^{3+}:$^4I_{13/2}$ → $^4I_{15/2}$	313–548	$417/T^2$	
$LiYF_4$:Yb/Er/Ce	980	Er^{3+}:$^4I_{13/2}$ → $^4I_{15/2}$	313–548	$532/T^2$	

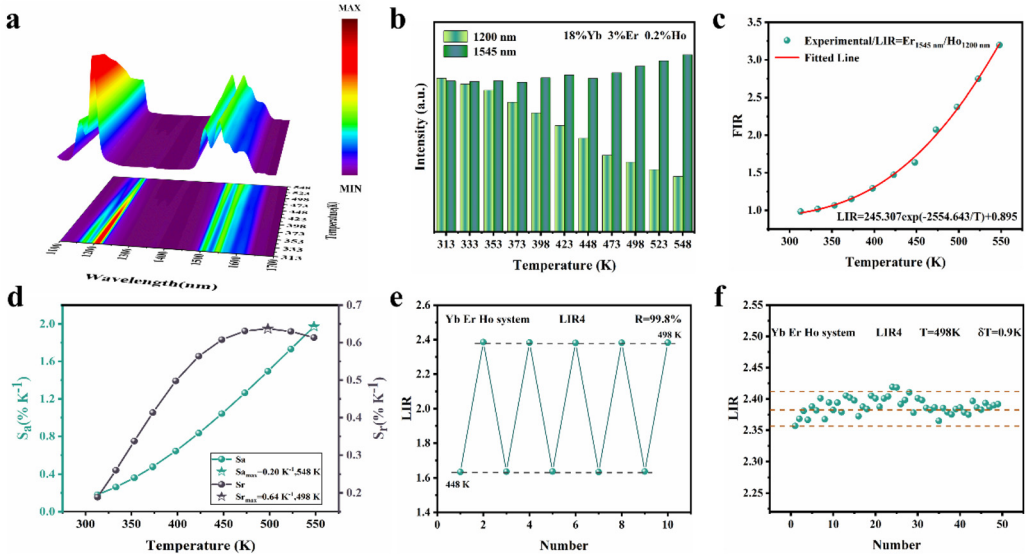

Fig. 7 (a) Temperature-dependent UC emission spectra of $LiYF_4$:18%Yb^{3+},3%Er^{3+},0.2%Ho^{3+} nanospheres under 980 nm excitation. (b) Summary of the integrated intensity of the emission of the thermally coupled levels in the $LiYF_4$:18%Yb^{3+},3%Er^{3+},0.2%Ho^{3+} nanospheres at different temperatures. (c) LIR values as a function of temperature. (d) S_r/S_a-temperature curves of the $LiYF_4$:18%Yb^{3+},3%Er^{3+},0.2%Ho^{3+} nanospheres. (e) LIR repeatability over five heating–cooling cycles. (f) LIR values measured 50 times continuously at 373 K.

slightly above 448 K. The intensity of the emission integrals is shown in Fig. 7b, and it indicated that as the temperature rose, the phonon vibration became active and participated in the Ho $^5I_6 \rightarrow$ Er $^4I_{13/2}$[40] energy transfer process, leading to an increase in the number of electrons in Er $^4I_{13/2}$ and a decrease in the number of electrons in Ho $^5I_6$. The two-part LIR was fitted using the non-thermal coupling formula:

$$\mathrm{LIR} = \frac{I_{1545}}{I_{1200}} = B\exp\left(\frac{C}{T}\right) + A \quad (24)$$

where I_{1545} and I_{1200} represent the emission intensity integrals of Er^{3+} and Ho^{3+}. A, B and C are fitting parameters, as shown in Fig. 7c. A, B and C were 0.89554, 245.30728 and −2554.64363, respectively. As shown in Fig. 7d, the $LiYF_4$:18%Yb^{3+},3%Er^{3+},0.2%Ho^{3+} nanospheres exhibited excellent S_r, reaching a maximum of 0.64% K^{-1} at 498 K (Table 3). The results of LIR repeatability over five heating–cooling cycles and 50 consecutive measurements of the LIR value at 498 K are shown in Fig. 7e and f, R = 99.8%, δT = 0.9 K. It was further demonstrated that the SFPE in the NIR-IIb offered excellent temperature readout performance in non-thermal coupling temperature measurement.

Table 3 Comparison of the temperature measurement performance of different materials

Compound	λ_{ex} (nm)	λ_{em} (nm)	T (K)	S_r (%K^{-1})	Ref.
LaF_3:Yb/Pr	980	978/1302	15–105	0.525	41
YVO_4:Yb/Er/Ho	980	1194/1545	313–573	0.166	40
$Y_3Al_5O_{12}$:Yb/Er/Ho	980	1194/1545	313–573	0.467	40
$BaTiO_3$:Yb/Er/Ho	980	1194/1545	313–573	0.4	40
$LiYF_4$:Yb/Er/Ho	980	1200/1545	313–548	0.64	This work

3. Conclusions

In summary, we have synthesized $LiYF_4$:Ln^{3+} with well-dispersed micron octahedral cones and nanosphere morphologies *via* a one-step hydrothermal synthesis. When $LiYF_4$ was singly doped with Er^{3+} ions, self-sensitized luminescence was accomplished under 381, 808 and 980 nm excitation. $LiYF_4$:18%Yb^{3+},2%Er^{3+} exhibited ultra-efficient photoluminescence in the visible region, showing 2.06 times higher green emission than that of commercial phosphors ($NaYF_4$:18%Yb^{3+},2%Er^{3+}). The two green thermally coupled energy levels of Er^{3+} demonstrated high relative sensitivity (1107/T^2). The transition of the $^4I_{13/2}$ split Stark sublevel (S_{1-7}) to the $^4I_{15/2}$ split Stark sublevel (X_{1-8}) of the Er^{3+} ion displayed SFPE in the NIR-IIb, and the relative sensitivity based on the thermal coupling Stark sublevel was 450/T^2, which is higher than any previously reported relative sensitivity for Er^{3+} SFPE. Co-doping with Ce^{3+} ions to give $LiYF_4$:18%Yb^{3+},2%Er^{3+},2%Ce^{3+} increased the NIR-IIb emission intensity by a factor of 3.07, and the relative sensitivity increased to 531/T^2. When co-doped with Ho^{3+} ions ($LiYF_4$:18%Yb^{3+},2%Er^{3+},0.2%Ho^{3+}), during non-thermally coupled temperature measurements of the characteristic emission of Ho^{3+} ions in NIR-II and the SFPE of Er^{3+} ions in NIR-IIb, the relative sensitivity reached a maximum value of 0.64% K^{-1} at 498 K, demonstrating its excellent temperature measurement performance at both thermally coupled and non-thermally coupled energy levels and making $LiYF_4$ a significant development in the field of bioimaging and nanomedicine.

4. Experimental section

LiF (A.R., Beijing Chemical Factory), NaF (A.R., Beijing Chemical Factory), $LiNO_3$ (A.R., Beijing Chemical Factory), NH_4F (G.R., Sinopharm Chemical Reagent Co., Ltd), $C_{10}H_{14}N_2O_8Na_2{\cdot}2H_2O$ (A.R., Aladdin), $Y(NO_3)_3{\cdot}6H_2O$ (A.R, Aladdin), $Yb(NO_3)_3{\cdot}6H_2O$ (A.R, Aladdin), $Er(NO_3)_3{\cdot}6H_2O$ (A.R, Aladdin), $Ho(NO_3)_3{\cdot}6H_2O$ (A.R, Aladdin), $Ce(NO_3)_3{\cdot}6H_2O$ (A.R, Aladdin).

4.1 Synthesis of $LiYF_4:Ln^{3+}$ (Ln = Er, Yb/Er) microcrystals

Normally, $Ln(NO_3)_3{\cdot}6H_2O$ (1 mmol) and LiF (4 mmol) were added in predetermined molar ratios to an empty beaker. Then, 10 ml deionized water was added dropwise, and the mixture was stirred continuously for 30 minutes to form a clear solution. NH_4F (32 mmol) was then dissolved in 20 ml deionised water in another empty beaker and stirred for 30 minutes. The previously clear solution was then slowly added and stirred 30 minutes before the mixture was poured into a Teflon-lined stainless-steel autoclave and stored at 200 °C for 24 hours. Finally, the prepared micron crystals were washed with deionized water and ethanol and precipitated using centrifugation. These samples were dehydrated at 60 °C for 24 h.

4.2 Synthesis of $LiYF_4:Ln^{3+}$ (Ln = Yb/Er, Yb/Er/Ho, Yb/Er/Ce) nanocrystals

The differences were that we replaced the reactant LiF with $LiNO_3$ (1 ml, 1 M), and the reaction time was adjusted to 6 h. Other processes were the same as above.

4.3 Synthesis of α-$NaYF_4$:18%Yb^{3+},2%Er^{3+} phosphors

First, $C_{10}H_{14}N_2O_8Na_2{\cdot}2H_2O$ (0.1 g), $Yb(NO_3)_3$ (1.8 ml 0.1 M), $Y(NO_3)_3$ (8 ml 0.1 M), and $Er(NO_3)_3$ (0.2 ml 0.1 M) were added to 10 ml deionized water and stirred for 30 minutes. Subsequently, NaF (2 mmol) and NH_4F (0.3 g) were added into the mixed solution, the pH was adjusted to 3, and the mixture was then stirred for 1 h. The mixture was then poured into a Teflon-lined stainless steel autoclave and stored at 120 °C for 24 hours. Finally, the α-$NaYF_4$:18%Yb^{3+},2%Er^{3+} phosphors were washed with deionized water and ethanol and precipitated by centrifugation. These samples were dehydrated at 60 °C for 24 h.

4.4 Synthesis of β-$NaYF_4$:18%Yb^{3+},2%Er^{3+} phosphors

The difference was that the reaction temperature was adjusted to 180 °C and the reaction time was 24 hours; the rest of the process was the same as that for α-$NaYF_4$:18%Yb^{3+},2%Er^{3+}.

4.4.1 Characterization. An X-ray diffractometer (SmartLab SE, Japan) with Cu K radiation (λ = 0.15405 nm) was used for the crystalline X-ray diffraction (XRD) analysis of all samples. A field-emission scanning electron microscope (SEM) (Regulus 8100, Hitachi,) with an operating voltage of 10 kV and a working distance of 12.3 nm was utilized to explore the surface morphology of the synthesized samples. An Andor Shamrock SR-750 spectrometer with a 980 nm/808 nm variable power laser (~15 W cm^{-2}), 75 W Xe lamp and an SR830 DSP lock-in amplifier and CCD detector (DS3-21312-112, and DS3-51412-0309 BWT Beijing Ltd) was used to capture the emission spectra of the prepared materials. The NIR emission spectra were captured using an Andor SR-500i spectrometer (Andor Technology Co, Belfast, U.K.). A temperature control system (TAP-02, orient-KOJI) and copper-constant thermocouple were used to complete the temperature sensing studies. Fourier transform infrared (FT-IR) spectroscopy was performed using a FT-IR spectrometer (VERTEX 80, Bruker). Diffuse reflectance spectra were obtained using a UV–vis spectrometer (Shimadzu UV-2450 spectrometer).

Author contributions

Kejie Li and Hanyu Xu designed, analysed, and experiments. Kejie Li wrote and revised manuscripts. Zhiying Wang and Mengmeng Dai assisted in performance testing. Zuoling Fu provided revision guidance, suggestions and financial support.

Conflicts of interest

There are no conflicts to declare.

Acknowledgements

This research was supported by the National Science Foundation of China (Grant No. 12374374), the Key Projects of Jilin Province Science and Technology Development Plan (Grant No. 20230201060GX) and the Graduate Innovation Fund of Jilin University (Grant No. 2023CX043). The authors would like to acknowledge the Instrument and Equipment Sharing Platform, college of physics (Jilin University) for testing assistance.

References

1 D. J. Naczynski, M. C. Tan, R. E. Riman and P. V. Moghe, Rare Earth Nanoprobes for Functional Biomolecular Imaging and Theranostics, *J. Mater. Chem. B*, 2014, **2**, 2958–2973.
2 Y. Zhou, C. Li and Y. Wang, Crystal–Field Engineering Control of an Ultraviolet–Visible–Responsive Near–Infrared–Emitting Phosphor and Its Applications in Plant Growth, Night Vision, and NIR Spectroscopy Detection, *Adv. Opt. Mater.*, 2022, **10**, 2102246.
3 E. Thimsen, B. Sadtler and M. Y. Berezin, Shortwave-infrared (SWIR) emitters for biological imaging: a review of challenges and opportunities, *Nanophotonics*, 2017, **6**, 1043–1054.
4 S. Yu, D. Tu, W. Lian, J. Xu and X. Chen, Lanthanide-doped near-infrared II luminescent nanoprobes for bioapplications, *Sci. China Mater.*, 2019, **62**, 1071–1086.

5 L. Wu, M. Jia, D. Li and G. Chen, Shell Engineering on Thermal Sensitivity of Lifetime-Based NIR Nanothermometers for Accurate Temperature Measurement in Murine Internal Liver Organ, *Nano Lett.*, 2023, **23**, 2862–2869.
6 A. Schroter, S. Märkl, N. Weitzel and T. Hirsch, Upconversion Nanocrystals with High Lanthanide Content: Luminescence Loss by Energy Migration versus Luminescence Enhancement by Increased NIR Absorption, *Adv. Funct. Mater.*, 2022, **32**, 2113065.
7 S. Tsuboi, S. Yamada, Y. Nakane, T. Sakata, H. Yasuda and T. Jin, Critical Review—Water-Soluble Near-Infrared Fluorophores Emitting over 1000 nm and Their Application to In Vivo Imaging in the Second Optical Window (1000–1400 nm), *ECS J. Solid State Sci. Technol.*, 2017, **7**, R3093–R3101.
8 S. Xu, S. Xiang, Y. Zhang, J. Zhang, X. Li, J. Sun, L. Cheng and B. Chen, 808 nm laser induced photothermal effect on Sm^{3+}/Nd^{3+} doped $NaY(WO_4)_2$ microstructures, *Sens. Actuators, B*, 2017, **240**, 386–391.
9 X. Jiang, C. Cao, W. Feng and F. Li, Nd^{3+}-doped $LiYF_4$ nanocrystals for bio-imaging in the second near-infrared window, *J. Mater. Chem. B*, 2016, **4**, 87–95.
10 X. Wang, X. Zhang, Y. Wang, H. Li, J. Xie, T. Wei, Q. Huang, X. Xie, L. Huang and W. Huang, Comprehensive studies of the Li^+ effect on $NaYF_4$:Yb/Er nanocrystals: morphology, structure, and upconversion luminescence, *Dalton Trans.*, 2017, **46**, 8968–8974.
11 T. Y. O. G. Chen, A. Kachynski, H. Ågren and P. N. Prasad, Intense visible and near-infrared upconversion photoluminescence in colloidal $LiYF_4:Er^{3+}$ nanocrystals under excitation at 1490 nm, *ACS Nano*, 2011, **5**, 4981–4986.
12 S. L. Maurizio, G. Tessitore, G. A. Mandl and J. A. Capobianco, Luminescence dynamics and enhancement of the UV and visible emissions of Tm^{3+} in $LiYF_4$: Yb^{3+},Tm^{3+} upconverting nanoparticles, *Nanoscale Adv.*, 2019, **1**, 4492–4500.
13 F. Carl, L. Birk, B. Grauel, M. Pons, C. Würth, U. Resch-Genger and M. Haase, $LiYF_4$:Yb/$LiYF_4$ and $LiYF_4$:Yb,Er/$LiYF_4$ core/shell nanocrystals with luminescence decay times similar to YLF laser crystals and the upconversion quantum yield of the Yb,Er doped nanocrystals, *Nano Res.*, 2020, **14**, 797–806.
14 W. Li, Q. He, J. Xu, C. Shao, S. Sun, S. Fan and L. Hu, Efficient NIR to NIR up-conversion in $LiYF_4:Yb^{3+}$,Tm^{3+} micro-octahedrons by modified hydrothermal method, *J. Lumin.*, 2020, **227**, 117396.
15 A. B. Andrade, G. F. C. Bispo, Z. S. Macedo and M. E. G. Valerio, Synthesis and characterization of luminescent Ln^{3+} (Ln = Eu, Tb and Dy)-doped $LiYF_4$ microcrystals produced by a facile microwave-assisted hydrothermal method, *J. Lumin.*, 2020, **219**, 116843.
16 Y. Song, R. Sun, G. Sun, Y. Xie and L. Sun, Upconversion/Downshifting Multimode Luminescence of Lanthanide-doped Nanocrystals for Multidimensional Information Encoding Security, *Chem. – Asian J.*, 2022, **17**(17), e202200537.
17 Y. Song, M. Lu, G. Mandl, Y. Xie, G. Sun, J. Chen, X. Liu, J. A. Capobianco and L. N. Sun, Energy Migration Control of Multimodal Emissions in an Er^{3+} -Doped Nanostructure for Information Encryption and Deep-Learning Decoding, *Angew. Chem., Int. Ed.*, 2021, **60**, 23790–23796.
18 S. Wang, J. Lin, Y. He, J. Chen, C. Yang, F. Huang and D. Chen, Remarkable laser-driven upconverting photothermal effect of Cs_3LnF_6@glass nanocomposites for anti-counterfeiting, *Chem. Eng. J.*, 2020, **394**, 124889.
19 L. Yan, J. Huang, Z. An, Q. Zhang and B. Zhou, Activating Ultrahigh Thermoresponsive Upconversion in an Erbium Sublattice for Nanothermometry and Information Security, *Nano Lett.*, 2022, **22**, 7042–7048.
20 Y. Xiao, X. Kuang, Y. Yeung and M. Ju, Investigation of the Structure and Luminescence Mechanism of Tm^{3+}-Doped $LiYF_4$: New Theoretical Perspectives, *Inorg. Chem.*, 2020, **59**, 1211–1217.
21 Y. Xiao, M. Ju, H. Yuan and Y. Yeung, Unveiling the Local Structure and Luminescence Mechanism of Er^{3+}-Doped $LiYF_4$: A Promising Near-Infrared Laser Crystal, *J. Phys. Chem. C*, 2021, **125**, 18015–18021.
22 K. Zhang, B. Wang, T. Liu, H. An, S. Deng, Z. Hu, Y. Kong and Q. Zeng, Sc dopant induced tailoring of persistent luminescence in $Na_3YSi_3O_9:Eu^{2+}$ for information recording, *J. Mater. Chem. C*, 2022, **10**, 15967–15980.
23 K. A. Denault, J. Brgoch, S. D. Kloss, M. W. Gaultois, J. Siewenie, K. Page and R. Seshadri, Average and local structure, debye temperature, and structural rigidity in some oxide compounds related to phosphor hosts, *ACS Appl. Mater. Interfaces*, 2015, **7**(2), 7264–7272.
24 L. E. Misiak and M. Subotowicz, Temperature EPR study of $LiY_{1-x}Yb_xF_4(Gd^{3+})$ single crystals, *Solid State Commun.*, 1991, **80**, 761–766.
25 S. Stojadinović, N. Tadić and R. Vasilić, Down-conversion photoluminescence of $ZrO_2:Er^{3+}$ coatings formed by plasma electrolytic oxidation, *Mater. Lett.*, 2018, **219**, 251–255.
26 N. Karayianis, Theoretical energy levels and g values for the 4I terms of Nd^{3+} and Er^{3+} in $LiYF_4$, *J. Phys. Chem. Solids*, 1971, **32**, 2385–2391.
27 M. D. Dramicanin, L. Marciniak, S. Kuzman, W. Piotrowski, Z. Ristic, J. Perisa, I. Evans, J. Mitric, V. Dordevic, N. Romcevic, M. G. Brik and C. G. Ma, Mn^{5+}-activated $Ca_6Ba(PO_4)_4O$ near-infrared phosphor and its application in luminescence thermometry, *Light: Sci. Appl.*, 2022, **11**, 279.
28 R. An, Y. Liang, R. Deng, P. Lei and H. Zhang, Hollow nanoparticles synthesized via Ostwald ripening and their upconversion luminescence-mediated Boltzmann thermometry over a wide temperature range, *Light: Sci. Appl.*, 2022, **11**, 217.
29 K. Zhu, Z. Wang, H. Xu and Z. Fu, Development of Multifunctional Materials Based on Heavy Concentration Er^{3+}–Activated Lead–free Double Perovskite $Cs_2NaBiCl_6$, *Adv. Opt. Mater.*, 2022, **10**, 2201182.
30 M. Jia, Z. Sun, M. Zhang, H. Xu and Z. Fu, What determines the performance of lanthanide-based ratiometric nanothermometers?, *Nanoscale*, 2020, **12**, 20776–20785.

31 S. Zhou, K. Deng, X. Wei, G. Jiang, C. Duan, Y. Chen and M. Yin, Upconversion luminescence of $NaYF_4$: Yb^{3+}, Er^{3+} for temperature sensing, *Opt. Commun.*, 2013, **291**, 138–142.

32 H. Zhang, X. Dong, L. Jiang, Y. Yang, X. Cheng and H. Zhao, Comparative analysis of upconversion emission of LaF_3:Er/Yb and LaOF:Er/Yb for temperature sensing, *J. Mol. Struct.*, 2020, **1206**, 127665.

33 X. Cheng, K. Yang, J. Wang, L. Yang and X. Cheng, Up-conversion luminescence and optical temperature sensing behaviour of Yb^{3+}/Er^{3+} codoped $CaWO_4$ material, *Opt. Mater.*, 2016, **58**, 449–453.

34 S. K. Singh, K. Kumar and S. B. Rai, Er^{3+}/Yb^{3+} codoped Gd_2O_3 nano-phosphor for optical thermometry, *Sens. Actuators, A*, 2009, **149**, 16–20.

35 G. Xiang, X. Liu, Q. Xia, X. Liu, S. Xu, S. Jiang, X. Zhou, L. Li, D. Wu, L. Ma, X. Wang and J. Zhang, Design of a bi-functional $NaScF_4$: Yb^{3+}/Er^{3+} nanoparticles for deep-tissue bioimaging and optical thermometry through Mn^{2+} doping, *Talanta*, 2021, **224**, 121832.

36 R. Lei, X. Liu, F. Huang, D. Deng, S. Zhao, H. Xu and S. Xu, Optical thermometry based on anomalous temperature-dependent 1.53 μm infrared luminescence of Er^{3+} in $BaMoO_4$: Er^{3+}/Yb^{3+} phosphor, *Opt. Mater.*, 2018, **86**, 278–285.

37 B. Cao, J. Wu, X. Wang, Y. He, Z. Feng and B. Dong, Multiple Temperature-Sensing Behavior of Green and Red Upconversion Emissions from Stark Sublevels of Er^{3+}, *Sensors*, 2015, **15**, 30981–30990.

38 Y. Shang, Q. Han, S. Hao, T. Chen, Y. Zhu, Z. Wang and C. Yang, Dual-Mode Upconversion Nanoprobe Enables Broad-Range Thermometry from Cryogenic to Room Temperature, *ACS Appl. Mater. Interfaces*, 2019, **11**, 42455–42461.

39 M. Quintanilla, Y. Zhang and L. M. Liz-Marzán, Subtissue Plasmonic Heating Monitored with CaF_2:Nd^{3+},Y^{3+} Nanothermometers in the Second Biological Window, *Chem. Mater.*, 2018, **30**, 2819–2828.

40 M. Jia, Z. Fu, G. Liu, Z. Sun, P. Li, A. Zhang, F. Lin, B. Hou and G. Chen, NIR–II/III Luminescence Ratiometric Nanothermometry with Phonon–Tuned Sensitivity, *Adv. Opt. Mater.*, 2020, **8**, 1901173.

41 A. M. Kaczmarek, M. K. Kaczmarek and R. Van Deun, Er^{3+}-to-Yb^{3+} and Pr^{3+}-to-Yb^{3+} energy transfer for highly efficient near-infrared cryogenic optical temperature sensing, *Nanoscale*, 2019, **11**, 833–837.